On Scene Flow Computation of Gas Structures with Optical Gas Imaging Cameras

Johannes Rangel Robert Schmoll Andreas Kroll
Department of Measurement and Control
University of Kassel, Germany
{johannes.rangel,robert.schmoll,andreas.kroll}@mrt.uni-kassel.de

Abstract

Gas leak inspection and gas leak quantification are nowadays of high relevance within the oil and gas industry as well as in many other industrial sectors. This has been driven by safety-related issues, economic losses and the considerable climate impact caused by such unwanted gas releases. Due to the latter, the efforts for developing new and more reliable measurement techniques for detecting and quantifying greenhouse gases such as methane have increased in the recent years. In this work, a stereo camera system based on optical gas imaging cameras is used for computing dense 3D velocity information, i.e. *scene flow, of escaping gas structures. Here, the optical flow, the disparity and the disparity change in likely gas image regions are computed utilizing classical variational methods. The accuracy of the applied methods and their applicability under real conditions in a biogas plant are characterized and tested. The results show that the recovered 3D gas velocity field per camera frame approaches the average 3D velocity field of the measured gas structure. The accuracy of the used method is affected, among others, when the imaged gas structures exhibit a low contrast.*

1. Introduction

Infrared (IR) cameras for gas visualization, also known as optical gas imaging (OGI) cameras, are used within industrial environments such as refineries, biogas plants and landfills, for spotting gas emissions without using active infrared sources. In the last years there have been efforts to enhance the capabilities of such devices for gas leak localization and quantification tasks with the help of image processing and data fusion techniques [4, 18, 21, 30]. The need for more accurate, effective and safe methods for gas leak detection and quantification has been motivated, on the one hand, by the international efforts for reducing the climate effects of gas emissions from the industry and, on the other hand, by the economic losses and safety problems caused by gas leaks. In this regard, the estimation of gas velocities using gas images has gained special attention, since this quantity is required for computing the emission flow rate.

Existing OGI-based methods for gas leak quantification estimate the gas velocity by computing the projected gas velocity in the images of a single OGI camera, *i.e*. by computing the optical flow in differential images [4, 6]. Here, the image plane and the main flow field direction are assumed to be parallel. However, this requirement is often violated due to the stochastic nature of gas flows in real scenarios, where external factors such as wind speed or sudden temperature changes occur. This leads to gas velocity estimates with a higher uncertainty when measuring under uncontrolled measurement conditions. A more robust and hence more reliable gas velocity estimation can be achieved by computing the 3D gas velocity field with a stereo gas camera system. The estimation of 3D velocity fields is also known as the scene flow problem and has been addressed in literature mainly for objects that can be measured in the visible spectrum [14, 26].

Due to the stochastic nature of gas flows under real conditions and the intrinsic characteristics of infrared cameras subject to their working principle, the scene flow problem for OGI cameras represents several challenges compared to the scene flow problem in the visual range. First of all, photometric consistency in the visible range is imposed in many computer vision problems, such as optical flow and stereo disparity, by assuming Lambertian object surfaces. While this assumption holds mainly for opaque objects in the visible range, it is violated when imaging semi-transparent or highly reflecting surfaces. In the case of semi-transparent fluids, photometric consistency can be assumed for predominant incompressible fluid flows or particle-seeded flows generated under controlled measurement conditions for particle image velocimetry (PIV) [13]. In that sense, the driving question for binocular scene flow computation in stereo gas images under real conditions relies on the required assumptions and the reliability of the computed data. Furthermore, spatial shifts in the images, also called jitter, originated by the integrated camera's cooling system, image noise, geometric and radiometric differences, temporal shifts between the two OGI cameras used and the influence of external factors such as wind speed, moving background objects and self occlusions [17] make the scene flow computation for gases more difficult.

In this work, a framework based on variational methods for estimating scene flow of gas emissions with two OGI cameras arranged in stereo configuration is proposed and evaluated. The practical use of the proposed framework focuses, among others, on the inspection and detection of unwanted gas releases in industrial environments, *e.g.* methane gas leaks within the oil and gas industry as well as renewables. Optical flow, disparity, disparity change and likely gas image regions are computed and used for computing the 3D gas flow fields. Special attention is given to the physical interpretation, accuracy and reliability of the computed information with the proposed method. For that, synthetic data and data acquired under real conditions are used.

2. Related Work

The problem of estimating 3D velocity fields from images is also known as the scene flow problem and has been addressed widely in the computer vision literature mainly for visible objects in different application fields such as autonomous driving, robotics and surveillance. An overview of the methods proposed to compute scene flow can be found in [14]. In general, scene flow approaches rely on geometric and photometric constraints assumed when using one or multiple views of the scene. For the case of binocular scene flow, the object's depth, depth change and motion has to be computed jointly or in a decoupled way by using the so-called stereokinematic constraints [15]. With these, 3D velocity vectors associated to the objects in the scene can be calculated pixelwise for each time frame. The fact that visible objects are assumed to be opaque, textured and may exhibit a rigid motion has given the chance to propose more accurate binocular scene flow approaches that exploit these assumptions [24].

Despite the progress in the last years for computing scene flow of visible objects, no applications on obtaining scene flow of gas structures under real conditions has been reported yet. In [28] a method for computing depth information of refractive flows such as hot air by using a stereo camera system and optical-flow-based features called refraction wiggles. However, the computed flow velocity is constrained to the image plane. Similarly, in [17] depth information of methane flows is obtained from a stereo OGI camera system. Here, spatio-temporal intensity changes in gas regions depicted in differential images were used for computing the depth information but no information regarding the velocity of the gas structures was given.

Based on the fact that gases and fluids in general are semi-transparent structures, tomographic approaches have been widely used in order to reconstruct their 3D motion and density distribution over time under controlled conditions. For this, multiple views of the fluid have to be taken simultaneously. In [12], for instance, a framework for computing 3D flow fields from multiple views of a particle-seeded volume under laboratory conditions is proposed. The fact that multiple views of the flow are available and that particle tracers are used, enables the use of tomographic approaches and enhances the accuracy of the fluid motion estimation and its 3D reconstruction. Nevertheless, these measurement conditions can be achieved mainly in elaborated laboratory setups, which reduces the applicability of the methods under real conditions. Watremez *et al.* [25] proposed a measurement setup based on 3 infrared cameras and tomographic methods for reconstructing the concentration distribution over time of methane emissions in industrial environments. However, no 3D gas velocity information was computed. Additionally, the cameras used have to be placed around the measured gas, which constrains the portability and applicability of the system.

Dynamic texture detection and 3D fire flame reconstruction are related applications to this work as well. In [1], a motion competition approach was proposed for segmenting dynamic image textures such as smoke or steam. Here, the segmented regions are characterized by the photometric assumptions used for computing the optical flow. In [27, 29], feature-based approaches for detecting smoke in visual images are presented. Block features such as local binary patterns or edge orientation histograms are used. Nevertheless, all these methods focus on the segmentation of the dynamic textures rather than on the accurate estimation of flow velocity. In [10, 19], stereo camera systems are used for gaining spatial information from fire flames. In these approaches, the fire flames are considered to be self emitting objects, *e.g.* opaque objects which surface can be reconstructed with a stereo camera system. Moreover, no 3D velocity information of the flames is recovered from the stereo images.

3. Working Principle

The intensity values of an OGI camera image $I(\boldsymbol{x}, t)$ at the pixel position $\boldsymbol{x} = (x, y)$ and time t are proportional to the radiant power received by the detector elements of the camera. Assuming the scene background as a black body (BB) and a fully transparent atmosphere within the spectral range of the camera, this relationship can be expressed as follows:

$$I(\boldsymbol{x}, t) \propto \Phi_{\mathrm{bg}}^{\mathrm{BB}}(\boldsymbol{x}, t)\tau_{\mathrm{g}}(\boldsymbol{x}, t) + \Phi_{\mathrm{g}}^{\mathrm{BB}}(\boldsymbol{x}, t)(1 - \tau_{\mathrm{g}}(\boldsymbol{x}, t)) \quad (1)$$

where $\Phi_{\mathrm{bg}}^{\mathrm{BB}}$ and $\Phi_{\mathrm{g}}^{\mathrm{BB}}$ are the black body radiant power of the background (bg) and the gas structure (g) respectively and τ_{g} is the gas transmittance detected by the detector element at the position $\boldsymbol{x}$ and time t. The value of τ_{g} is described by the Lambert-Beer Law, *i.e.* $\tau_{\mathrm{g}}(\boldsymbol{x},t) = e^{-\alpha_{\mathrm{g}}\bar{c}_{\mathrm{g}}(\boldsymbol{x},t)l_{\mathrm{g}}(\boldsymbol{x},t)}$, and depends on the absorption coefficient of the gas α_{g} and its average concentration $\bar{c}_{\mathrm{g}}$ over the measurement path length l_{g}. Under constant gas and background temperature and measuring with a fixed camera, differential images I^{diff} can be used for increasing the contrast of the gas wrt. its background:

$$I^{\mathrm{diff}}(\boldsymbol{x},t) \propto \left(\Phi_{\mathrm{bg}}^{\mathrm{BB}}(\boldsymbol{x},t) - \Phi_{\mathrm{g}}^{\mathrm{BB}}(\boldsymbol{x},t)\right)\tau_{\mathrm{g}}^{\mathrm{diff}}(\boldsymbol{x},t) \tag{2}$$

with $\tau_{\mathrm{g}}^{\mathrm{diff}}(\boldsymbol{x},t) = \tau_{\mathrm{g}}(\boldsymbol{x},t) - \tau_{\mathrm{g}}(\boldsymbol{x},t+1)$. Several conclusions can be drawn from (2). First, the intensity changes observed in I^{diff} are proportional to the temperature difference between the gas and the background and created by gas concentration and gas expansion changes arising from mixing processes with its surroundings. Secondly, stereo differential images can be used for recovering spatial information from gas structures when $\tau_{\mathrm{g}}^{\mathrm{diff}}$ is similar, *i.e.* photometrically consistent, in the field of view (FOV) of both cameras [17]. Here, it is assumed that photometrically consistent gas regions can be observed in consecutive differential images as well as in stereo differential images as long as the gas velocity can be sampled with the frame rate of the camera. Based on this, 3D gas velocity fields can be computed pixelwise with stereo differential gas images by combining the optical flow and the stereo matching problem under the photometric consistency assumption.

Consider a non-stationary gas structure with velocity $\boldsymbol{V}_{\mathrm{g}}$ observed simultaneously by two fixed OGI cameras. The optical centers of the left (L) and right (R) camera are placed at O_{L} and O_{R}, respectively (see Figure 1). The horizontal distance between the cameras is defined by the baseline b. Considering three different time instants $t_0 = t$, $t_1 = t+1$ and $t_2 = t+2$, two pairs of consecutive differential images, *i.e.* $I_{\mathrm{L/R}}^{\mathrm{diff}}$ at t_0 and t_1, can be created. Corresponding spatio-temporal gas concentration and flow changes that emerge in differential images can be described by using following assumptions [26]:

$$\begin{aligned}
&\text{a. } \underbrace{I_{\mathrm{R}}^{\mathrm{diff}}(\boldsymbol{x}_{\mathrm{L}}+\boldsymbol{p}_{\mathrm{L}},t_0) - I_{\mathrm{L}}^{\mathrm{diff}}(\boldsymbol{x}_{\mathrm{L}},t_0)}_{E_1} = 0\\
&\text{b. } \underbrace{I_{\mathrm{L}}^{\mathrm{diff}}(\boldsymbol{x}_{\mathrm{L}}+\boldsymbol{w}_{\mathrm{L}},t_1) - I_{\mathrm{L}}^{\mathrm{diff}}(\boldsymbol{x}_{\mathrm{L}},t_0)}_{E_2} = 0\\
&\text{c. } \underbrace{I_{\mathrm{R}}^{\mathrm{diff}}(\boldsymbol{x}_{\mathrm{L}}+\boldsymbol{p}_{\mathrm{L}}+\boldsymbol{p}'_{\mathrm{L}}+\boldsymbol{w}_{\mathrm{L}},t_1) - I_{\mathrm{R}}^{\mathrm{diff}}(\boldsymbol{x}_{\mathrm{L}}+\boldsymbol{p}_{\mathrm{L}},t_0)}_{E_3} = 0\\
&\text{d. } \underbrace{I_{\mathrm{R}}^{\mathrm{diff}}(\boldsymbol{x}_{\mathrm{L}}+\boldsymbol{p}_{\mathrm{L}}+\boldsymbol{p}'_{\mathrm{L}}+\boldsymbol{w}_{\mathrm{L}},t_1) - I_{\mathrm{L}}^{\mathrm{diff}}(\boldsymbol{x}_{\mathrm{L}}+\boldsymbol{w}_{\mathrm{L}},t_1)}_{E_4} = 0
\end{aligned} \tag{3}$$

Here, $\boldsymbol{p}_{\mathrm{L}}(\boldsymbol{x}_{\mathrm{L}}) = (d_{\mathrm{L}}(\boldsymbol{x}_{\mathrm{L}}),0)$ is the disparity field, $d_{\mathrm{L}}(\boldsymbol{x}_{\mathrm{L}})$ is the disparity, $\boldsymbol{p}'_{\mathrm{L}}(\boldsymbol{x}_{\mathrm{L}}) = (d'_{\mathrm{L}}(\boldsymbol{x}_{\mathrm{L}}),0)$ is the change of the disparity field wrt. the next frame, $d'_{\mathrm{L}}(\boldsymbol{x}_{\mathrm{L}})$ the disparity change and $\boldsymbol{w}_{\mathrm{L}}(\boldsymbol{x}_{\mathrm{L}}) = (u_{\mathrm{L}}(\boldsymbol{x}_{\mathrm{L}}), v_{\mathrm{L}}(\boldsymbol{x}_{\mathrm{L}}))$ is the optical flow in the left camera. Notice also that $\boldsymbol{x}_{\mathrm{R}} = \boldsymbol{x}_{\mathrm{L}} + \boldsymbol{p}_{\mathrm{L}}$ in Figure 1. The data term E_1 relates to the epipolar constraint in stereo images, E_2 and E_3 relate to the optical flow constraint in each camera and E_4 describes the disparity flow constraint. The computation of $\boldsymbol{w}_{\mathrm{L}}$, $\boldsymbol{p}_{\mathrm{L}}$ and $\boldsymbol{p}'_{\mathrm{L}}$ can be carried out either separately as proposed in [20] or jointly. For the joint estimation of $\boldsymbol{w}_{\mathrm{L}}$, $\boldsymbol{p}_{\mathrm{L}}$ and $\boldsymbol{p}'_{\mathrm{L}}$, the constraints expressed in (3) are combined partly or completely within an optimization framework [8, 26].

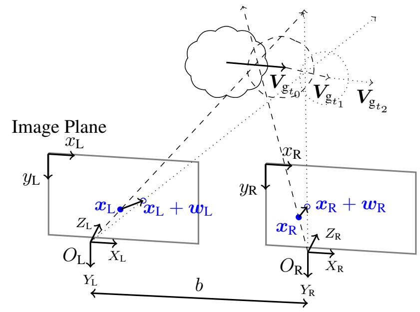

Figure 1. Measurement setup for computing 3D gas velocity fields.

With $\boldsymbol{w}_{\mathrm{L}}$, $\boldsymbol{p}_{\mathrm{L}}$ and $\boldsymbol{p}'_{\mathrm{L}}$ a pixelwise 3D gas velocity vector field $\boldsymbol{V}(\boldsymbol{x}_{\mathrm{L}})$ in $\mathrm{m\,s^{-1}}$ wrt. O_{L} can be obtained as follows:

$$\underbrace{\begin{bmatrix} V_X(\boldsymbol{x}_{\mathrm{L}}) \\ V_Y(\boldsymbol{x}_{\mathrm{L}}) \\ V_Z(\boldsymbol{x}_{\mathrm{L}}) \end{bmatrix}}_{\boldsymbol{V}(\boldsymbol{x}_{\mathrm{L}})} = f \cdot b \cdot \begin{bmatrix} \frac{x_{\mathrm{L}}-x_0+u_{\mathrm{L}}(\boldsymbol{x}_{\mathrm{L}})}{d_{\mathrm{L}}(\boldsymbol{x}_{\mathrm{L}})+d'_{\mathrm{L}}(\boldsymbol{x}_{\mathrm{L}})} - \frac{x_{\mathrm{L}}-x_0}{d_{\mathrm{L}}(\boldsymbol{x}_{\mathrm{L}})} \\ \frac{y_{\mathrm{L}}-y_0+v_{\mathrm{L}}(\boldsymbol{x}_{\mathrm{L}})}{d_{\mathrm{L}}(\boldsymbol{x}_{\mathrm{L}})+d'_{\mathrm{L}}(\boldsymbol{x}_{\mathrm{L}})} - \frac{y_{\mathrm{L}}-y_0}{d_{\mathrm{L}}(\boldsymbol{x}_{\mathrm{L}})} \\ \frac{s}{d_{\mathrm{L}}(\boldsymbol{x}_{\mathrm{L}})+d'_{\mathrm{L}}(\boldsymbol{x}_{\mathrm{L}})} - \frac{s}{d_{\mathrm{L}}(\boldsymbol{x}_{\mathrm{L}})} \end{bmatrix} \tag{4}$$

where (x_0, y_0) is the principal point of the left image in px, s is the camera constant in px, b the stereo baseline in m and f the camera frame rate in Hz. It is worth mentioning that the computed 3D velocity field corresponds to the path-averaged and concentration-weighted 3D velocity field of the measured gas structure. This means that $\boldsymbol{V}$ belongs to a virtual surface that is placed in the average 3D position of the observed gas [17].

In general, just a region of the 3D velocity field calculated with (4) is of interest for post-processing tasks such as mean gas velocity estimation or flow rate estimation. The gas detection limit of OGI cameras, also called noise equivalent concentration length (NECL), given in $\mathrm{ppm\,m}$, is related to a gas boundary in the image, where the gas signal cannot be differentiated from the camera noise anymore. An image segmentation approach can be applied to compute this boundary.

4. Measurement System and Methods

In this application, the measurement system consists of two OGI cameras, arranged with parallel image planes, which work within the spectral range of 3.2 - $3.4\ \mathrm{\mu m}$. In this

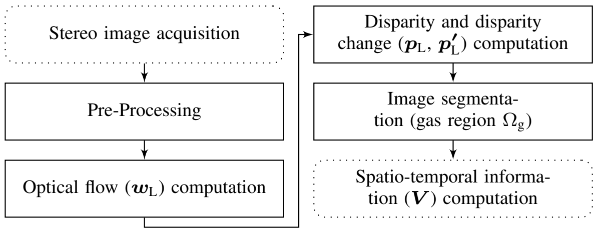

Figure 2. Processing steps for estimating spatio-temporal information of gas flows from a stereo OGI camera system.

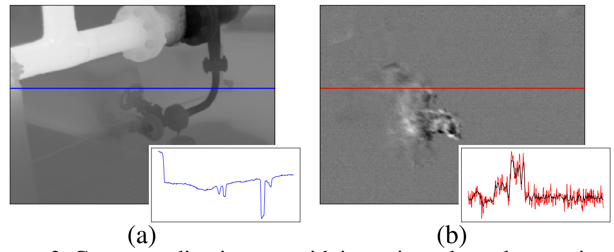

Figure 3. Corresponding images with intensity values along an image row, (a) raw and (b) differential. The effect of the used smoothing filter in the differential image is depicted as well (black curve).

particular range, volatile organic compounds (VOC) such as methane (CH_4) or butane (C_4H_{10}) absorb part of the incoming infrared radiation. The used images have a size of $m \times n = 240 \times 320$ px, the camera constant is $s = 780$ px and the camera's frame rate is $f = 30$ Hz. The baseline b of the stereo setup is variable and is set between 0.2 - 0.65 m.

In order to compute spatio-temporal information of the measured gas structures by using (4), the acquired images have to undergo a pipeline of processing steps (see Figure 2 and following sections). Here, it is proposed to compute the optical flow, disparity and disparity change fields by using classical variational methods together with a multi-scale optimization approach. In the first step, $\boldsymbol{w}_{\mathrm{L}}$ is computed alone. In a second step, $\boldsymbol{d}_{\mathrm{L}}$ and $\boldsymbol{d}'_{\mathrm{L}}$ are computed jointly using $\boldsymbol{w}_{\mathrm{L}}$. Additionally, image regions with likely gas information are extracted for further evaluation by using a variational segmentation approach based on level sets.

The decoupled computation of the optical flow from the disparities is motivated by several reasons. First, it is assumed that disparities tend to be larger than the optical flow. Therefore, it is expected that less scaled image representations are needed for computing the optical flow. Since variational methods with multi-scale strategy exhibit larger computation errors when dealing with small image structures that exhibit larger motions [23], the number of scaled representations used plays an important role. Secondly, decoupling the computation of the optical flow from the disparity and disparity changes reduces the computational complexity of the algorithms and hence increases the efficiency of the data processing framework [15].

4.1. Pre-Processing Step

The calibration of the stereo camera system enhances the accuracy of the computed data due to the correction of systematic errors that the system may exhibit. In this application geometric and radiometric discrepancies between the cameras are corrected by estimating the intrinsic and extrinsic camera parameters as well as their radiometric characteristic curves as described in [16]. Temporal shifts between the camera images cannot be fully avoided in the current setup since the used OGI cameras cannot be triggered simultaneously. Nevertheless, image timestamps are used for evaluating stereo images with small time shifts.

The rectified images are used to create differential images (see Fig. 3) as described in (2). These are normalized to $[0, 1]$. Due to the fact that OGI cameras use a cooling engine to guarantee the necessary detector sensitivity for gas detection, small spatial shifts in sub-pixel range or jitter can be observed in the differential images. Here, the jitter effect on differential gas images is reduced by image registration [21].

In a final pre-processing step, the stochastic spatial noise in the differential images is reduced. Several tests have shown that energy-based denoising approaches are more appropriate for preserving gas structures in differential images while reducing the spatial noise. Figure 3b shows the filtered information from an image row (red line) with an energy-based denoising filter with Sobolev prior [11].

4.2. Optical Flow Computation

The projected gas motion $\boldsymbol{w}_{\mathrm{L}}$ in the differential gas images of the left OGI camera is computed by using a classical variational method and the numerical approach proposed by Brox *et al.* in [3], where the following objective function is minimized for a given image domain Ω by using a multi-scale approach:

$$E_{\mathrm{OF}}(\boldsymbol{w}_{\mathrm{L}}) = \int_{\Omega} \psi\left(|E_2|^2\right) + \beta\psi\left(|\nabla E_2|^2\right) + \alpha\psi\left(S_{\mathrm{OF}}\right) d\boldsymbol{x}_{\mathrm{L}} \quad (5)$$

with $S_{\mathrm{OF}} = |\nabla u_{\mathrm{L}}|^2 + |\nabla v_{\mathrm{L}}|^2$. The first term relates to the brightness constancy assumption for differential gas images (see (3a)), the second term with $\nabla = (\partial/\partial x, \partial/\partial y)$ accounts for spatial gradient similarities between the images and the third term imposes smoothness on the 2D flow field $\boldsymbol{w}_{\mathrm{L}}$. The factors α and β weight the terms for the smoothness constraint and the gradient constancy, respectively, and the function $\psi(r^2) = \sqrt{r^2 + \epsilon^2}$ with $\epsilon = 0.001$ reduces the influence of outliers during the minimization.

4.3. Disparity and Scene Flow Computation

The computation of the disparity and the disparity change per stereo image pair wrt. the left image is carried out jointly by minimizing the following objective function:

$$E_{\mathrm{SF}}(\boldsymbol{p}_{\mathrm{L}}, \boldsymbol{p}'_{\mathrm{L}}) = \int_{\Omega} \gamma_1 \psi \left(|\nabla d_{\mathrm{L}}|^2\right) + \gamma_2 \psi \left(\left|\nabla d'_{\mathrm{L}}\right|^2\right) d\boldsymbol{x}_{\mathrm{L}} + \int_{\Omega} \psi \left(|E_1|^2\right) + \psi \left(|E_3|^2\right) + \psi \left(|E_4|^2\right) d\boldsymbol{x}_{\mathrm{L}} \tag{6}$$

where γ_1 and γ_2 penalize the smoothness of the disparity field and disparity change field, respectively. The objective function (6) is minimized in a similar fashion as for the optical flow. It can be observed that E_{SF} only depends on $\boldsymbol{p}_{\mathrm{L}}$ and $\boldsymbol{p}'_{\mathrm{L}}$ since $\boldsymbol{w}_{\mathrm{L}}$ was computed previously. In order to avoid local minima during the minimization of (6), a minimum disparity d_0 has to be given as initialization parameter.

The quality of the computed optical flow, disparities and disparity changes can be quantified pixelwise by evaluating the assumptions from (6) and the imposed smoothness constraint on the disparity and the disparity change:

$$U_{\mathrm{SF}}(\boldsymbol{x}_{\mathrm{L}}) = \gamma_1 \psi \left(|\nabla d_{\mathrm{L}}|^2\right) + \gamma_2 \psi \left(\left|\nabla d'_{\mathrm{L}}\right|^2\right) + \psi \left(|E_1|^2\right) + \psi \left(|E_3|^2\right) + \psi \left(|E_4|^2\right) \tag{7}$$

The values of $U_{\mathrm{SF}}(\boldsymbol{x}_{\mathrm{L}})$ are low or close to zero when the stereokinematic assumptions hold and are directly related to the uncertainty of the computed data. However, their range may vary depending on the measurement scene and the image intensity values. Additionally, homogeneous image regions or regions without texture information may exhibit lower $U_{\mathrm{SF}}(\boldsymbol{x}_{\mathrm{L}})$ values than image regions with gas information. To avoid the effect of untextured regions on the quality measure, the coefficient $c_{U_{\mathrm{SF}}}$ is computed per frame over a defined region Ω_{g} as follows:

$$c_{U_{\mathrm{SF}}} = |\Omega_{\mathrm{g}}|^{-1} \sum_{\Omega_{\mathrm{g}}} e^{-U_{\mathrm{SF}}(\boldsymbol{x}_{\mathrm{L}})} \tag{8}$$

where $|\Omega_{\mathrm{g}}|$ is the number of pixels in Ω_{g}. The image region Ω_{g} is described as a region of interest (ROI), in which gas structures are present, and its computation is described in the next section.

4.4. Image Segmentation with Gas Information

The approaches presented in sections 4.2 and 4.3 allow obtaining pixelwise information over the image domain Ω. In practice, captured gas structures do not cover the entire FOV of the OGI cameras and hence just a part of the differential gas image is of interest. The segmentation of the differential gas images is not a trivial problem since external moving objects and sudden radiation or temperature changes in the measured scene may cause misleading results. For the sake of simplicity and for further evaluation of the computed spatio-temporal information about the measured gas structures, it is assumed that motion and image intensity distribution are sufficient features for separating gas segments from the image background. Based on this,

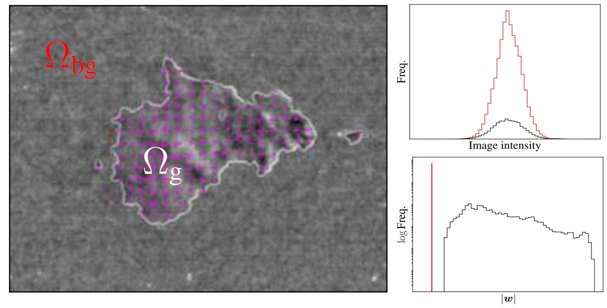

(a) (b)

Figure 4. (a) Segmentation of differential image with the used approach and optical flow (magenta). (b) Image intensity (top), *i.e.* I^{diff} and logarithm of normed optical flow (bottom), *i.e.* $|\boldsymbol{w}|$, distribution in image regions Ω_{g} (black) and Ω_{bg} (red).

the following objective function is used for segmenting differential gas images in two regions $\Omega = \Omega_{\mathrm{g}} \cup \Omega_{\mathrm{bg}}$:

$$E_{\mathrm{ROI}}(\Phi(\boldsymbol{x}_{\mathrm{L}})) = \nu \int_{\Omega} |\nabla H(\Phi)| d\boldsymbol{x}_{\mathrm{L}} - \int_{\Omega} H(\Phi) \log q_{\mathrm{g}}^{\mathrm{diff}} d\boldsymbol{x}_{\mathrm{L}} - \int_{\Omega} (1 - H(\Phi)) \log q_{\mathrm{bg}}^{\mathrm{diff}} d\boldsymbol{x}_{\mathrm{L}} \tag{9}$$

where $\Omega_{\mathrm{g}} \cap \Omega_{\mathrm{bg}} = \emptyset$, $q_i^{\mathrm{diff}}(I^{\mathrm{diff}}, u, v) = q_i(I^{\mathrm{diff}}) q_i(u) q_i(v)$ for $i \in \{\mathrm{g}, \mathrm{bg}\}$, H is a smoothed version of the Heaviside function and $\Phi(\boldsymbol{x}_{\mathrm{L}})$ is an embedding function, which is positive within Ω_{g} and negative within Ω_{bg}. $q_i(k)$ is the probability density function that models the distribution of image intensities I^{diff} and horizontal u and vertical motions v within the region indexed by i. Here, q_i is assumed as the normal distribution (see Figure 4). As in the previous sections, E_{ROI} is minimized by using gradient descent and a multi-scale strategy. The use of more sophisticated approaches for segmenting objects such as machine-learning-based algorithms are out of the scope of this work.

5. Experiments

In order to quantify the accuracy and reliability of the used approach compared to alternative methods, several tests were carried out by using synthetic and real data. Several field measurements were carried out and evaluated for assessing the applicability of the system.

In a first step, suitable parameters α and β for the optical flow computation were found by using benchmark data from the Middlebury dataset [2] (see Table 1). The averaged Euclidean distance, also called 2D averaged endpoint error (AEE), between the computed and the ground truth optical flow was used as error metric. Table 1 shows that α has a more significant effect on the accuracy of the optical flow than β for the tested dataset. It is also observed that the used method exhibits a slightly larger AEE compared to other optical flow strategies such as Farnebäck [5] or FlowNet 3.0 with pre-trained weights [9]. Nevertheless,

Table 1. Optical flow's AEE in px for used method (Brox) and for different parameters α and β in three benchmark scenes: (Dimetrodon, Hydrangea, Urban2) [2]. Results for the Farnebäck (Fbck) and FlowNet 3.0 (FN3) methods are also presented.

Brox				Fbck	FN3
α	$\beta = 1.0$	$\beta = 0.5$	$\beta = 0.01$		
0.5	$(0.7, 0.7, 7.0)$	$(0.8, 1.3, 7.3)$	$(0.9, 1.6, 7.5)$	(0.3, 0.2, 0.9)	(0.2, 0.3, 0.4)
0.1	$(0.4, 0.5, 1.4)$	$(0.4, 0.5, 1.1)$	$(0.4, 0.5, 1.1)$		
0.05	$(0.3, 0.5, 1.2)$	$(0.3, 0.5, 1.1)$	$(0.4, 0.5, 1.1)$		
0.01	$(0.4, 0.8, 1.5)$	$(0.4, 0.7, 1.2)$	$(0.4, 0.5, 1.1)$		

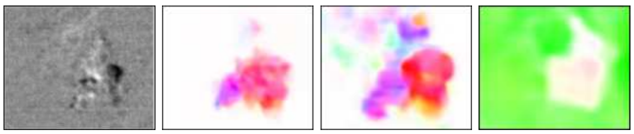

(a) (b) (c) (d)

Figure 5. Color encoded optical flow computation on real differential gas images with different methods. (a) Differential image, optical flow: (b) Brox, (c) Farnebäck and (d) FlowNet 3.0 with pre-trained weights .

previous tests on real differential images have shown that the used method is more suitable for differential gas images due to its robustness against image noise (see Fig. 5). Taking the previous tests into account, the parameters γ_1 and γ_2, are set to be within a range of the same order of magnitude than α and β. For the further experiments, α, β, γ_1 and γ_2 were set to 0.05, 0.1, 0.05 and 0.5 respectively. The parameter ν for segmenting the image was set empirically through previous tests to 0.5 for all experiments.

5.1. Synthetic Data

A simulation environment for generating synthetic stereo images of dynamic fluids was developed for evaluating the reliability of the computed optical flow, 3D gas position and the 3D gas velocity under ideal conditions (*i.e.* no lens distortion, no jitter, no radiometric differences between the cameras, zero spatial noise and stationary background). The algorithm proposed in [22] was used for generating three different dynamic flows and hence three different stereo differential image sequences (S) of an incompressible buoyant fluid within a volume of $100 \times 100 \times 100$ voxels, with voxel size of $4\,\mathrm{mm}^3$, for 11 time steps of $1\,\mathrm{ms}$ and flow velocities within the range $[0, 6.5]\,\mathrm{m\,s^{-1}}$. Concentration and 3D velocity information per voxel were obtained at each time step. A volume ray casting approach and pre-defined geometric parameters of the stereo camera system (camera constant $s = 780\,\mathrm{px}$, baseline $b = 0.2\,\mathrm{m}$) were used for projecting the path-averaged and concentration-weighted 3D gas velocities $\boldsymbol{V}^*(\boldsymbol{x})$ and 3D gas positions into stereo images. The image size was set to $320 \times 240\,\mathrm{px}$. Considering a distance between gas volume and stereo camera system of about $2\,\mathrm{m}$, optical flows up to $2.5\,\mathrm{px}$ per frame are expected.

The differences between the three image sequences are shown in Table 2. The magnitude of the mean 3D flow velocity per frame $|\boldsymbol{V}^*_{\text{avg}}|$, the directional angles[1] of the mean 3D flow per frame, *i.e.* $\theta^*_{\text{avg}_X}$, $\theta^*_{\text{avg}_Y}$ and $\theta^*_{\text{avg}_Z}$, the standard deviation of the pixelwise velocity magnitude per frame $\sigma_{|\boldsymbol{V}^*(\boldsymbol{x})|}$ and the number of pixels N occupied by the gas within the left image were averaged over all sequence frames for characterizing each image sequence. The orientation angle can be considered as the main difference. Nevertheless the second sequence differs the most from the other two.

Table 2. Characteristic information of used synthetic sequences.

S	$\overline{\lvert\boldsymbol{V}^*_{\text{avg}}\rvert}$ / $\mathrm{mm\,s^{-1}}$	$(\overline{\theta^*_{\text{avg}_X}}, \overline{\theta^*_{\text{avg}_Y}}, \overline{\theta^*_{\text{avg}_Z}})$ / °	$\overline{\sigma}_{\lvert\boldsymbol{V}^*(\boldsymbol{x})\rvert}$ / $\mathrm{mm\,s^{-1}}$	$\overline{N}$ / px
1	3265.3	$(86.7, 175.97, 92.26)$	1382.0	8088.2
2	**2667.3**	$\mathbf{(71.0, 161.0, 89.3)}$	**972.8**	**7491.4**
3	2683.8	$(101.3, 160.4, 105.8)$	1248.7	8023.3

After generating stereo differential images for each sequence, a 3D velocity field $\boldsymbol{V}(\boldsymbol{x})$ was computed per frame with the approach proposed in section 4.3. The decoupled method for scene flow computation presented in [20] was also used for comparing the results. For the latter, the optical flow methods after Brox and Farnebäck together with the semi-global matching method (SGM) [7] for disparity computation were considered. Following evaluation metrics were used for assessing the results:

$$\mathrm{RMVE} = 100\,\% \cdot \left| \frac{|\boldsymbol{V}^*_{\text{avg}}| - |\boldsymbol{V}_{\text{avg}}|}{|\boldsymbol{V}^*_{\text{avg}}|} \right| \quad \text{3D AEE} = \frac{\sum_{\Omega_{\mathrm{g}}} |\boldsymbol{V}^* - \boldsymbol{V}|}{|\Omega_{\mathrm{g}}|}$$
$$\mathrm{AEMV} = \cos^{-1}\left(\frac{\boldsymbol{V}^*_{\text{avg}} \cdot \boldsymbol{V}_{\text{avg}}}{|\boldsymbol{V}^*_{\text{avg}}||\boldsymbol{V}_{\text{avg}}|} \right) \quad \text{3D AAE} = \frac{\sum_{\Omega_{\mathrm{g}}} \cos^{-1}\left(\frac{\boldsymbol{V}^* \cdot \boldsymbol{V}}{|\boldsymbol{V}^*||\boldsymbol{V}|} \right)}{|\Omega_{\mathrm{g}}|} \tag{10}$$

where RMVE is the absolute value of the relative mean velocity error per frame in $\%$, AEMV is the angular error of mean velocity per frame in px, 3D AEE is the 3D average endpoint error per frame in px and 3D AAE is the 3D averaged angular error per frame in $^\circ$. For the 3D AEE and 3D AAE, the 3D flow field between three consecutive synthetic raw frames was used as reference $\boldsymbol{V}^*(\boldsymbol{x})$. Additionally, the distribution of the computed 3D flow field components per frame, *i.e.* $V_X(\boldsymbol{x})$, $V_Y(\boldsymbol{x})$ and $V_Z(\boldsymbol{x})$, was compared with the distribution of the reference flow field components by calculating the corresponding correlation factor $\overline{r}_{\mathrm{SF}_{X/Y/Z}}$ between their histograms. For that, the histogram value range was set to $[0, \max(V^*_{X/Y/Z_i})]$ and divided in 50 bins for each frame i. The performance of the segmentation approach for gas structures was tested as well. For that, the ratio (SA) between the segmented image region with likely gas information and the reference gas region was used.

As depicted in Table 3, a smaller RMVE can be achieved with the proposed approach compared to the alternative methods tested. In addition, the average magnitude and direction of the measured flow field per frame was computed

[1]Directional angles are defined as the inverse cosine of each normalized vector component.

Table 3. Assessment of computed 3D flow field of synthetic gas images. The values of the error metrics were averaged over whole sequence.

s	Proposed Method							SGM+Brox	SGM+Fbck
	$\overline{\text{RMVE}}$ / %	$\overline{\text{AEMV}}$ / °	3D $\overline{\text{AEE}}$ / mm s^{-1}	3D $\overline{\text{AAE}}$ / °	$\overline{c_{U\text{SF}}}$	$\overline{\text{SA}}$ / %	$(\bar{r}_{\text{SF}_X}, \bar{r}_{\text{SF}_Y}, \bar{r}_{\text{SF}_Z})$	$\overline{\text{RMVE}}$ / %	$\overline{\text{RMVE}}$ / %
1	6.56 ± 5.65	12.20 ± 5.41	72.00	33.79	0.92	58.31	$(0.68, 0.79, 0.73)$	16.06 ± 5.51	36.07 ± 2.37
2	$\mathbf{15.35 \pm 4.52}$	11.61 ± 5.98	66.78	30.84	0.91	67.57	$(0.56, 0.74, 0.56)$	35.31 ± 8.05	46.74 ± 6.25
3	9.60 ± 4.30	11.59 ± 5.35	72.43	34.09	0.90	71.40	$(0.44, 0.73, 1.00)$	47.10 ± 14.70	65.81 ± 9.30

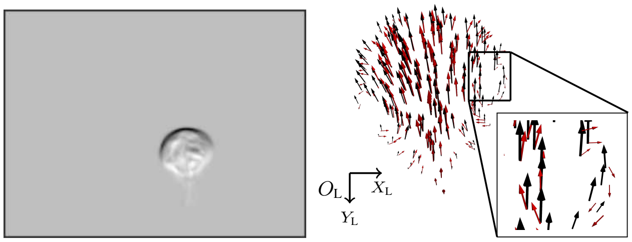

(a) (b)

Figure 6. Synthetic differential image 3D gas flow field for third dataset with reference (red) and computed flow field (dark).

with a relative error up to 10 % for the first and third sequence. The RMVE for the second sequence is relatively large (up to 15 %). Considering that the velocities in the reference 3D flow field of the second sequence vary less than in the other sequences, less texture variations in the differential images are produced. Untextured image regions affect directly the optical flow and disparity computation and therefore lead to an increased error.

As the calculated 3D AEE, 3D AAE, r_{SF} and figure 6b show, the 3D gas velocity fields recovered with stereo differential images agree with the dominant gas velocity and direction of the reference. However, small flow variations cannot be reconstructed. This can be observed through the large angle errors in the pixelwise assessment and the relatively low correlation factor between the magnitudes of the two fields.

5.2. Field Measurements

The performance of the measurement system and the proposed method for computing 3D gas velocity fields was evaluated under real measurement conditions in a biogas facility (see Figure 7). For this, methane was released from a nozzle at a distance of approx. 6 m away from the stereo OGI camera system with a baseline of $b = 0.65$ m. Additionally, a 3D ultrasonic anemometer was placed next to the nozzle for measuring the wind speed and direction with a sampling rate of 5 Hz. Here, it is assumed that the methane flow field captured by the camera system is dominated by the wind speed and direction. Moving objects in the background were avoided during the experiment for enhancing the image segmentation. It is worth mentioning that measured wind speed with the anemometer cannot be taken directly as a reference due to the placement of the anemometer wrt. the nozzle.

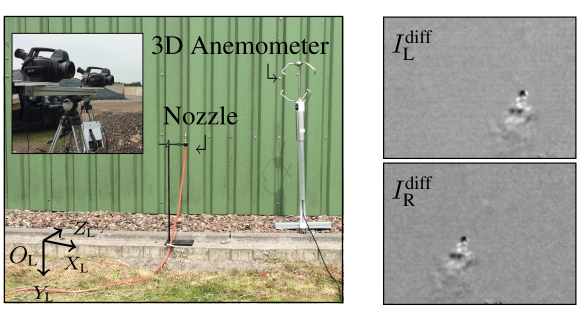

(a) (b)

Figure 7. Field measurement setup. (a) Equipment used and (b) exemplary stereo differential image after pre-processing step.

Table 4 shows the mean velocity vector $\boldsymbol{V}_\text{avg}$ and the mean directional angles $(\theta_{\text{avg}_X}, \theta_{\text{avg}_Y}, \theta_{\text{avg}_Z})$ per frame measured with the system for three image sequences (S), each consisting of 500 frames. The image regions considered for evaluating the mean velocity vector were extracted by using the proposed segmentation method. The mean wind velocity $|\boldsymbol{V}^*_\text{avg}|$ and mean wind direction $(\theta^*_{\text{avg}_X}, \theta^*_{\text{avg}_Y}, \theta^*_{\text{avg}_Z})$ per sequence measured with the anemometer are presented as well. First of all, it can be observed that the magnitude of $|\boldsymbol{V}_\text{avg}|$ is underestimated (see Table 4) when comparing with $|\boldsymbol{V}^*_\text{avg}|$. Nevertheless, the joint computation of the disparity and disparity changes in stereo differential images leads to smoother results with $c_{U_\text{SF}} \approx 0.8$ within the segmented image region with gas information when comparing with the decoupled scene flow method SGM+Brox (see Figure 8). It is also observed that the computed velocity and direction values approach the wind speed and direction over time. Due to the discrepancy regarding the sampling rates between the cameras and the anemometer, sudden wind velocity and direction changes can be seen in the measured velocities with the camera system (see Figure 8a). The measurement uncertainty of the proposed system regarding the obtained 3D velocity fields is subject to systematic geometric, radiometric and temporal inaccuracies of the cameras. Besides this, the discrepancy between the computed mean velocities and the measured wind speed during the experiments is mainly caused by inaccuracies in the optical flow computation in gas regions with poor contrast, segmented image regions with no gas information and the spatial offset between the nozzle and the anemometer.

Table 4. Measurement results from field experiments.

s	Gas (stereo OGI camera system)					Wind (3D anemometer)	
	Proposed method			SGM+Brox			
	$\lvert\overline{\boldsymbol{V}_{\mathrm{avg}}}\rvert$ / m s^{-1}	$(\overline{\theta_{\mathrm{avg}\,X}}, \overline{\theta_{\mathrm{avg}\,Y}}, \overline{\theta_{\mathrm{avg}\,Z}})$ / °	$\overline{c_{U}}_{\mathrm{SF}}$	$\lvert\overline{\boldsymbol{V}_{\mathrm{avg}}}\rvert$ / m s^{-1}	$(\overline{\theta_{\mathrm{avg}\,X}}, \overline{\theta_{\mathrm{avg}\,Y}}, \overline{\theta_{\mathrm{avg}\,Z}})$ / °	$\lvert\overline{\boldsymbol{V}^{*}_{\mathrm{avg}}}\rvert$ / m s^{-1}	$(\overline{\theta^{*}_{\mathrm{avg}\,X}}, \overline{\theta^{*}_{\mathrm{avg}\,Y}}, \overline{\theta^{*}_{\mathrm{avg}\,Z}})$ / °
1	0.73 ± 0.25	$(87.5, 74.4, 81.2)$	0.84	0.80 ± 0.35	$(98.02, 76.09, 75.25)$	1.20 ± 0.45	$(87.53, 82.27, 117.98)$
2	0.82 ± 0.33	$(115.09, 85.72, 123.45)$	0.83	1.12 ± 4.72	$(126.06, 86.98, 111.34)$	1.52 ± 0.5	$(112.24, 94.06, 154.30)$
3	0.80 ± 0.33	$(115.27, 72.24, 131.25)$	0.82	0.76 ± 0.33	$(123.61, 74.90, 92.24)$	0.98 ± 0.5	$(106.39, 84.59, 123.89)$

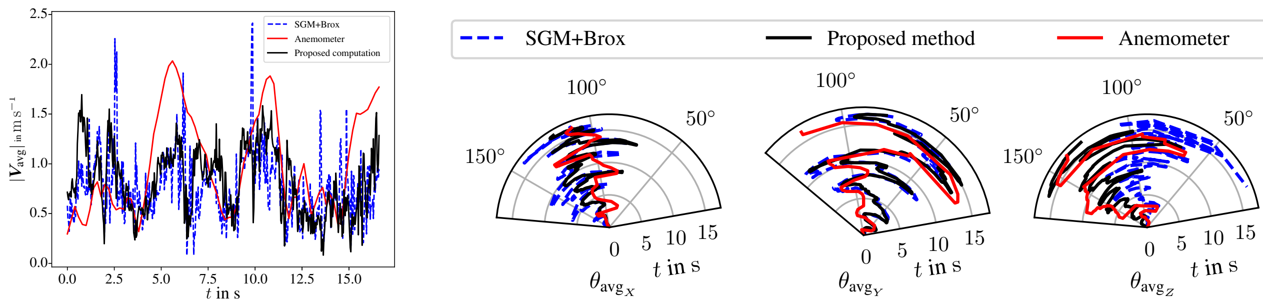

(a) (b)

Figure 8. Results obtained in field experiments for image sequence 3 wrt. (a) gas velocity magnitude and (b) directional angles over time.

6. Discussion

The application of variational methods for computing the scene flow in stereo differential images with gas information has shown to be adequate but constrained by photometric and geometric assumptions. In this regard, it has been observed that mean 3D velocity profiles can be computed with the proposed approach and can be used for gas inspection applications where the main flow characteristics of the escaping gas are of importance. The tests on synthetic data have shown that small variations in the 3D flow or in the concentration distribution cannot be measured in a reliable way with the system. When building differential images, small spatio-temporal gas concentration changes do not create a significant change in the measured radiant power captured by the camera detectors. For this reason, laminar gas flows cannot be fully measured with this approach. Untextured gas regions can also occur when the thermal contrast between the observed gas and its background is low or the gas concentration along the measurement path is reduced.

Besides the photometric assumptions needed for computing the scene flow in differential gas images, it has also been shown that the joint computation of the disparity and the disparity change reduces the variance of the computed 3D velocity fields. In this regard, the smoothness constraints used for computing $\boldsymbol{w}_{\mathrm{L}}$, $\boldsymbol{p}_{\mathrm{L}}$, and $\boldsymbol{p}'_{\mathrm{L}}$ are suitable for gas textures due to the natural smooth gas concentration transitions between the gas boundaries and the image background. It is important to mention that the weighting parameters α, β, $\gamma_{1/2}$ and ν have an effect on the accuracy of the method and suitable values may depend on the measurement conditions.

As for the scene flow computation, the performance of the segmentation approach is affected by the contrast of the gas textures in the differential images. Gas regions with low contrast are likely to be labeled as background. On the other hand, moving objects in the scene such as flies, trees or clouds may be assigned to the gas regions due to their movement. These outliers have a direct effect on the accuracy of the estimated mean gas velocity and mean gas direction. Further gas descriptors such as motion parameters could be used for enhancing the performance of the image segmentation.

7. Conclusions

In this work, the computation of 3D gas velocity fields, *i.e.* scene flow, by using differential images from a stereo OGI camera system was presented and tested. For this, a data processing framework was used, where the optical flow, the disparity and the disparity change in the measured scene are computed. It was shown that the obtained 3D gas velocity field relies on a mean virtual surface placed inside the measured gas and represents the dominant velocity components of the real gas flow. Additionally, a simplified image segmentation approach is used for deriving image regions with likely gas information. By this, most of the background information that causes misleading results is suppressed. In general, the accuracy of the proposed method is affected by systematic errors due to geometric, radiometric and temporal offsets in the measurement system and by the measurement conditions. Field experiments in a biogas facility have shown the applicability of the system under real measurement conditions.

Acknowledgment. The authors would like to thank the German Environmental Foundation (DBU) (no. 20015/379) and the German Federal Ministry for Economic Affairs and Energy (BMWi) (no. 03THW10K17) for supporting this project as well as FLIR Systems GmbH for providing a test camera.

References

[1] T. Amiaz, S. Fazekas, D. Chetverikov, and N. Kiryati. Detecting regions of dynamic texture. In *1st Int. Conf. on Scale Space and Variational Methods in Computer Vision (SSVM)*, volume 4485, pages 848–859, Ischia, Italy, May 2007.

[2] S. Baker, D. Scharstein, J. Lewis, S. Roth, M. Black, and R. Szeliskil. A database and evaluation methodology for optical flow. *Int. Journal of Computer Vision*, 92(1):1–31, Mar. 2011.

[3] T. Brox, A. Bruhn, N. Papenberg, and J. Weickert. High accuracy optical flow estimation based on a theory for warping. *European Conf. on Computer Vision (ECCV)*, 3024:25–36, 2004.

[4] S. Dierks and A. Kroll. Quantification of Methane Gas Leakages using Remote Sensing and Sensor Data Fusion. In *IEEE Sensors Applications Symposium (SAS)*, Glassboro, USA, Mar. 2017.

[5] G. Farnebäck. Two-frame motion estimation based on polynomial expansion. In *Proceedings of the 13th Scandinavian Conf. on Image Analysis*, LNCS 2749, pages 363–370, Gothenburg, Schweden, June 2003.

[6] M. Gålfalk and D. Bastviken. Remote sensing of methane and nitrous oxide fluxes from waste incineration. *Waste Management*, 75:319–326, 2018.

[7] H. Hirschmüller and D. Scharstein. Evaluation of cost functions for stereo matching. In *IEEE Conf. on Computer Vision and Pattern Recognition (CVPR)*, Minneapolis, MN, 2007.

[8] F. Huguet and F. Devernay. A variational method for scene flow estimation from stereo sequences. In *IEEE Int. Conf. on Computer Vision (ICCV)*, Rio de Janeiro, Brazil, Oct. 2007.

[9] E. Ilg, T. Saikia, M. Keuper, and T. Brox. Occlusions, motion and depth boundaries witha generic network for disparity, optical flow or scene flow estimation. In *European Conf. on Computer Vision (ECCV)*, Munich, Germany, Sept. 2018.

[10] B. C. Ko, J.-H. Jung, and J.-Y. Nam. Fire Detection and 3D Surface Reconstruction Based on Stereoscopic Pictures and Probabilistic Fuzzy Logic. *Fire Safety Journal*, 68(Supplement C):61–70, Aug. 2014.

[11] K. Lakshmi, R. Parvathy, S. Soumya, and K. P. Soman. Image denoising solutions using heat diffusion equation. In *Int. Conf. on Power, Signals, Controls and Computation*, Thrissur, Kerala, India, Jan. 2012.

[12] K. Lasinger, C. Vogel, and K. Schindler. Volumetric flow estimation for incompressible fluids using the stationary stokes equations. In *IEEE Int. Conf. on Computer Vision (ICCV)*, Venice, Italy, Oct. 2017.

[13] T. Liu and L. Shen. Fluid Flow and Optical Flow. *Journal of Fluid Mechanics*, 614(11):253–291, 2008.

[14] M. Menze, C. Heipke, and A. Geiger. Object scene flow. *ISPRS Journal of Photogrammetry and Remote Sensing*, 140:60–76, 2018.

[15] A. Mitichea and J. Aggarwal. *Computer Vision Analysis of Image Motion by Variational Methods*. Springer International Publishing, 2014.

[16] J. Rangel and A. Kroll. Characterization and Calibration of a Stereo Gas Camera System for Obtaining Spatial Information of Gas Structures. In *IEEE Sensors Applications Symposium (SAS)*, Seoul, Korea, Mar. 2018.

[17] J. Rangel and A. Kroll. On Obtaining Reliable Spatial Information from Gas Structures with a Stereo Camera System. In *Int. Conf. on Sensing Technology (ICST)*, Limerick, Ireland, Dec. 2018.

[18] M. A. Rodriguez-Conejo, J. Melendez, R. Barber, and S. Garrido. Design of an Infrared Imaging System for Robotic Inspection of Gas Leaks in Industrial Environments. *Int. Journal of Advanced Robotic Systems*, 12(23), Mar. 2015.

[19] L. Rossi, T. Molinier, M. Akhloufi, Y. Tison, and A. Pieri. A 3D vision system for the measurement of the rate of spread and the height of fire fronts. *Measurement Science and Technology*, 21(10), Aug. 2010.

[20] R. Schuster, C. Bailer, O. Wasenmüller, and D. Stricker. Combining stereo disparity and optical flow for basic scene flow. In *Commercial Vehicle Technology Symposium (CVT-18)*, Kaiserslautern, Germany, Mar. 2018.

[21] S. Soldan and A. Kroll. Towards Automated Gas Leak Detection Using IR Gas Imaging Cameras. In *Advanced Infrared Technology and Applications (AITA)*, Turin, Italy, Sept. 2013.

[22] J. Stam. Stable Fluids. In *Proceedings of the 26th annual conference on Computer graphics and interactive techniques*, pages 121–128. ACM Press/Addison-Wesley Publishing Co., July 1999.

[23] F. Steinbruecker, T. Pock, and D. Cremers. Advanced data terms for variational optic flow estimation. In *Vision, Modeling and Visualization (VMV)*, Braunschweig, Germany, 2009.

[24] C. Vogel, K. Schindler, and S. Roth. 3d scene flow estimation with a piecewise rigid scene model. *Int. Journal of Computer Vision*, 115(1):1–28, Oct. 2015.

[25] X. Watremez, N. Labat, G. Audouin, X. M. Bertrand Lejay, D. Dubucq, A. Marblé, P.-Y. Foucher, L. Poutier, R. Danno, D. Elie, and M. Chamberland. Remote Detection and Flow rates Quantification of Methane Releases Using Infrared Camera Technology and 3D Reconstruction Algorithm. In *SPE Annual Technical Conf. and Exhibition*, Dubai, UAE, Sept. 2016.

[26] A. Wedel and D. Cremers. *Stereo Scene Flow for 3D Motion Analysis*. Springer, 2011.

[27] X. Wu, X. Lu, and A. Leung H. A video based fire smoke detection using robust adaboost. *Sensors*, 18(11):3780, 2018.

[28] T. Xue, M. Rubinstein, N. Wadhwa, A. Levin, F. Durand, and W. T. Freeman. Refraction wiggles for measuring fluid depth and velocity from video. In *European Conf. on Computer Vision (ECCV)*, Zurich, Switzerland, Sept. 2014.

[29] F. Yuan. Video-based smoke detection with histogram sequence of LBP and LBPV pyramids. *Fire Safety Journal*, 46(3):132–139, 2011.

[30] Y. Zeng, J. Morris, A. Sanders, S. Mutyala, and C. Zeng. Methods to determine response factors for infrared gas imagers used as quantitative measurement devices. *Journal of the Air & Waste Management Association*, 67(11):1180–1191, 2017.